JGR Space Physics

RESEARCH ARTICLE
10.1029/2023JA031540

Solar Wind Control of Hemispherically-Integrated Field-Aligned Currents at Earth

A. L. Fleetham[1], S. E. Milan[1], S. M. Imber[1], and S. K. Vines[2]

[1]School of Physics and Astronomy, University of Leicester, Leicester, UK, [2]Johns Hopkins University Applied Physics Laboratory, Laurel, MD, USA

Key Points:

- The field-aligned current (FAC) flow increases with increasing southward interplanetary magnetic field (IMF) B_z
- There is a steeper gradient of increase for IMF B_z values below −10 nT than for that above 10 nT, for all local times
- Features of polar cap potential saturation are observed in FAC data during strong southward IMF

Correspondence to:

A. L. Fleetham,
Alf21@leicester.ac.uk

Citation:

Fleetham, A. L., Milan, S. E., Imber, S. M., & Vines, S. K. (2023). Solar wind control of hemispherically-integrated field-aligned currents at Earth. *Journal of Geophysical Research: Space Physics*, *128*, e2023JA031540. https://doi.org/10.1029/2023JA031540

Received 30 MAR 2023
Accepted 15 JUL 2023

Abstract Magnetic reconnection occurring between the interplanetary magnetic field (IMF) and the dayside magnetopause causes a circulation of magnetic flux and plasma within the magnetosphere, known as the Dungey cycle. This circulation is transmitted to the ionosphere via field-aligned currents (FACs). The magnetic flux transport within the Dungey cycle is quantified by the cross-polar cap potential (CPCP or transpolar voltage). Previous studies have suggested that under strong driving conditions the CPCP can saturate near a value of 250 kV. In this study we investigate whether an analogous saturation occurs in the magnitudes of the FACs, using observations from the Active Magnetosphere and Planetary Electrodynamics Response Experiment. The solar wind speed, density and pressure, the B_z component of the IMF, and combinations of these, were compared to the concurrent integrated current magnitude, across each hemisphere. We find that FAC magnitudes are controlled most strongly by solar wind speed and the orientation and strength of the IMF. FAC magnitude increases monotonically with solar wind driving but there is a distinct knee in the variation around IMF $B_z = -10$ nT, above which the increase slows.

Plain Language Summary During extreme space weather events, the threat to space-based and surface infrastructure has become of increasing concern within the past 2 decades. These space weather events are directly responsible for electrical currents flowing in the ionosphere that produce potentially dangerous magnetic field perturbations on the ground. With this motivation, we use satellite magnetometer data in order to gain greater insight into the field aligned current systems present above both poles of the Earth. With many mechanisms and processes which govern the magnitude of these currents (and associated potentials) still being widely disputed, we hope to offer verification of whether or not these currents saturate at high solar wind driving, in order to create a clearer picture of the behavior of these systems from nominal to intense space weather conditions.

1. Introduction

The magnetosphere of Earth is known to have dynamic interactions with the interplanetary magnetic field (IMF) flows constantly outward from the Sun, embedded within the solar wind. Opposing magnetic polarities of the dayside magnetosphere and the IMF most efficiently drive the cycle of magnetic field lines breaking and reconnecting, known as the Dungey Cycle (Dungey, 1961), which drives a circulation of magnetic flux and plasma within the magnetosphere. Reconnection ant the magnetopause eventually leads to the onset of magnetic reconnection in the magnetotail, and the competition between these two processes leads to changes in the location and size of the auroral zones (Cowley & Lockwood, 1992; Siscoe & Huang, 1985). Field-aligned currents (FACs), first proposed by Birkeland (1908, 1913), communicate stress from the magnetosphere to the ionosphere, producing the ionospheric convection pattern. The theorized current systems were later confirmed via satellite and terrestrial observations in the work of Cummings and Dessler (1967), with further work carried out by Iijima and Potemra (1976). Detailed investigations were then undertaken by Iijima and Potemra (1976) and Iijima and Potemra (1978), offering an insight into the structure of these current systems. The studies indicated that the footprint of these FACs formed two broken concentric rings around both poles of Earth. The inner ring, or the Region 1 (R1) current system, connects the ionosphere to the magnetopause and the outer ring, or region 2 (R2) current system, connects to the partial ring current and inner magnetosphere.

Observations of the strength of ionospheric convection, parameterized by the cross polar cap potential (CPCP), are often used as a measure of the strength of solar wind-magnetosphere coupling. Under normal conditions the CPCP is found to be approximately linearly related to the solar wind motional electric field, once corrected

for IMF clock angle which modulates the reconnection geometries available at the magnetopause (Khachikjan et al., 2008). However, it is observed that under particularly strong driving conditions the CPCP saturates (Hairston et al., 2005; Russell et al., 2001; Shepherd, 2007). Several competing theories have been put forward to explain saturation, including induced magnetospheric magnetic fields opposing that of the magnetopause, limiting the global reconnection rate, and Alfvén wave impedance (mis-)matching at the ionosphere (Gao et al., 2013; Kivelson & Ridley, 2008; Siscoe et al., 2002). A significant hurdle, however, to better understanding this phenomenon is the relative rarity of sufficiently strong solar wind driving conditions and the difficulty of accurately measuring the CPCP at such times. Measurements of the CPCP by low Earth orbit spacecraft, such as those of Defense Meteorological Satellite Program, and by ground-based ionospheric radars, such as the Super Dual Auroral Radar Network, can be unreliable during geomagnetically disturbed conditions. In this study we use observations of the FACs measured by the Active Magnetosphere and Planetary Electrodynamics Response Experiment (AMPERE) as a diagnostic for convection strength.

Many studies have employed AMPERE data to study how FAC systems evolve in response to the solar wind conditions (e.g., (Anderson et al., 2008, 2014; Carter et al., 2016; Clausen et al., 2012; Waters et al., 2004)), nonetheless the investigation of an analogous FAC saturation- to that which is seen with CPCP- has yet to be studied in depth. Initial studies, such as that undertaken by Anderson and Korth (2007), have suggested that the saturation seen within the CPCP, is also seen in the FACs. Their study employed engineering magnetic field data from the Iridium Communications Network satellite constellation from 1999 to 2003 and looked at the evolution of FACs during instances of geomagnetic storms. In this study, we also use data from AMPERE, in tandem with solar wind observations from the OMNI data set, to investigate the FAC systems over both hemispheres, with increasing solar wind driving. Building on this previous study, we employ AMPERE data from the 7 years of 2010 to 2016. By not limiting the data analyzed to just storm-time conditions, we provide a fuller picture of how the integrated current magnitude behaves in response to increasing solar wind driving from nominal to extreme conditions.

2. Data Sets

The AMPERE data set comprises polar maps of FAC density derived from magnetometer observations made onboard satellites of the Iridium telecommunications constellation (Anderson et al., 2002, 2021; Waters et al., 2001, 2020). Measured perturbations from the background magnetic field are inverted with Ampére's law to retrieve the FAC density on a grid of 24 hr of magnetic local time and 50 1-degree magnetic latitude bins, over both northern and southern polar regions. The AMPERE-derived FAC distributions are comprised of a 10-min interval of observations that span the polar regions. The FAC patterns can then be produced at a 2-min cadence using a sliding 10-min accumulation window (Anderson et al., 2002; Waters et al., 2020).

The aim of this study is to determine the relationship between AMPERE observations of FACs and upstream solar wind conditions. The solar wind parameters considered were the solar wind speed, density and pressure, and the Geocentric Solar Magnetospheric B_y and B_z components of the IMF at the nose of the bowshock, all provided by the OMNI data set (King & Papitashvili, 2005). From these we derived the Y-component of the motional electric field of the solar wind, $E_y = -V_{sw}B_z$, a measure of the magnetic flux transported within the solar wind toward the magnetosphere which can reconnect with Earth's dipole. This is defined such that when $E_y > 0$ reconnection is expected at low to mid-latitudes across the dayside magnetopause which opens magnetic flux and drives the Dungey cycle; when $E_y < 0$ then reconnection is expected to occur at the high latitude magnetopause, tailwards of the cusps, known as lobe reconnection (e.g., Fuselier, 2021 and references therein). In addition to the individual solar wind parameters, the Milan et al. (2012) coupling parameter provides an estimation of the dayside reconnection rate:

$$\Phi_D = \Lambda V_x^{\frac{4}{3}} B_{YZ} \sin^{\frac{9}{2}} \frac{1}{2}\theta \tag{1}$$

Here, Λ is a constant of proportionality with the value 3.3×10^5 $\mathrm{m}^{\frac{2}{3}}$ $\mathrm{s}^{\frac{2}{3}}$. V_x is the absolute magnitude of the x-component of the solar wind velocity and B_{yz} is defined as $B_{yz} = \sqrt{(B_y^2 + B_z^2)}$, such that $V_x B_{yz}$ gives the transport of magnetic flux per unit length, transverse to the flow direction. Finally, θ is the IMF clock angle. When combined in this way, these parameters give an approximation of the subsolar reconnection rate, which drives

the Dungey cycle, and is zero for purely northwards IMF. The analysis covers the 2010 to 2016 time period (inclusive) and aims to capture all the currents associated with the electrodynamics of magnetosphere-ionosphere coupling.

3. Observations

From the AMPERE data, we determined the integrated FAC in both the northern and southern hemispheres at 2-min cadence. AMPERE provides FAC density on a 24×50 grid in both hemispheres, with positive and negative current densities representing upward and downward FACs, respectively. In this paper we present the results from the northern hemisphere only. The analysis was performed for the southern hemisphere, also, however the results were very similar, though the FAC magnitudes were somewhat lower, as reported by Coxon et al. (2016). The FACs are expected to be in balance such that the total FAC flowing into each hemisphere should be zero, so we treated upward and downward FACs separately. The area of each grid cell was calculated, multiplied by the FAC density in that cell, and then summed over the grid to provide a measure of the total upward and total downward FAC. Any current density of less than 0.1 μA m^{-1} was not included within the analysis, as this is close to the noise floor of the AMPERE technique. We found, as expected, that the magnitudes of the integrated upward and downward FACs were equal, and henceforth just the total FAC magnitude was used (the sum of the absolute upward and downward FAC). To determine how current magnitude varied in response to different solar wind parameters, the total current was plotted against each solar wind parameter, in addition to E_y and Φ_D. Initially the analysis of these parameters was separated by year and month to determine if any seasonal or solar cycle trends were present. The FAC magnitudes differed with season due to variations in solar-insolation of the polar regions and hence conductance (Coxon et al., 2016). However, all showed the same behavior, and we have therefore combined together the data, from all years and months, to increase statistical significance.

3.1. Quadrants and Direction of Current

We next tested to see if the response of the FACs to the solar wind differed in different local time sectors. We divided the observations into four quadrants, encompassing 03–09 MLT (dawn), 09–15 MLT (noon), 15–21 MLT (dusk), and 21–03 MLT (midnight). We then found the total upward and downward FACs in each of these quadrants. From previous studies of FACs associated with different solar wind driving conditions (Ganushkina et al., 2018; Iijima & Potemra, 1976; Milan et al., 2017), the R1 and R2 FACs are expected to be mainly contained in the dawn and dusk quadrants, R0 FACs in the noon quadrant, and substorm currents in the midnight quadrant. Figure 1 shows typical examples of FAC distributions for northward and southward IMF, with pink lines demarcating the four quadrants. On the left panel of Figure 1, the northward IMF regime is shown. During this time, the solar wind conditions were a high magnitude, positive B_z component value, in addition to a B_y component that fluctuated around positive and negative values of low magnitude. The solar wind speed and densities were nominal, at approximately 420 km s^{-1} and under 10 cm^{-3}, respectively. Under these conditions, with a northward IMF, the currents are located at high latitudes, predominantly confined to the noon quadrant. The currents show a quadrupolar configuration of upward and downward FACs which is typical of reverse lobe convection cells driven by lobe reconnection (Fear, 2021; Milan et al., 2020; Zanetti et al., 1984). The right panel of Figure 1 shows the southward IMF regime. The conditions at this time consisted of prolonged negative (southward) IMF B_z component and B_y component that fluctuated with low magnitude between positive and negative values. The solar wind speed was measured to be below average at approximately 370 km s^{-1}, conversely the solar wind density was elevated at just under 30 cm^{-3}. For southward IMF the FACs are seen at lower latitudes and generally have the region 1/region 2 configuration first described by Iijima and Potemra (1976), which is associated with standard twin-cell convection driven by subsolar reconnection. In the example shown in Figure 1 (right panel) there is little current flowing in the noon quadrant for this particular example, however R0 FACs often appear here when B_y is non-zero (Ohtani et al., 1995; Saunders, 1989). A more complicated pattern is seen in the midnight quadrant, where FACs associated with the Harang discontinuity are usually seen (Erickson et al., 1991). As these typical current patterns are so different, for many aspects of the subsequent analysis, we subdivided the data set into observations for which $B_z > 0$ and $B_z < 0$.

Within the top panel of Figure 2, the average variation in the FAC magnitude in the northern hemisphere as a function of IMF B_z, in bins 1 nT wide, for 2010–2016 is presented. The FAC in each quadrant is shown by the colored lines and the total FAC by the black line. Standard deviations of the variation are also calculated, and

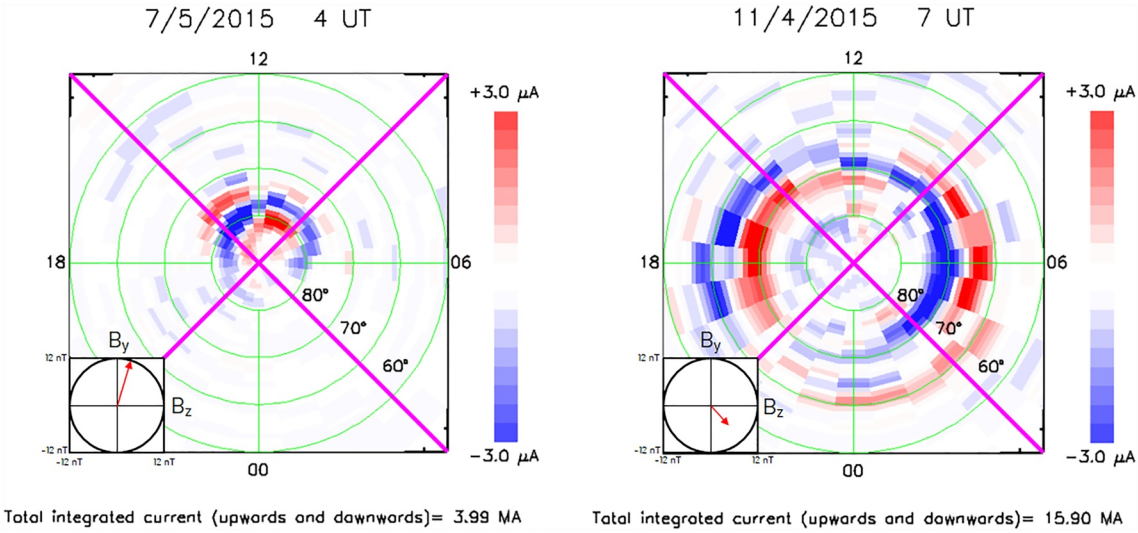

Figure 1. Current systems present above the northern hemisphere of Earth during periods of northwards (left) and southwards (right) interplanetary magnetic field (IMF) occurring on 7th May 2015 and 11th April 2015, respectively. The flow of current, toward or away from the Earth, is indicated in the blue and red shading, respectively. The pink lines indicate the division into 4 local time quadrants that was employed for the study. The insert (bottom left of each plot) shows a representation of the IMF orientation at the time of the current map.

presented in the same format for each quadrant in the middle panel. The lower panel shows the number of points per bin. The FACs are a minimum for small B_z and increase as B_z becomes more negative and more positive. The increase in each quadrant is approximately linear in the range $-15 > B_z > 15$ nT. Deviations from this quasi-linearity are discussed further below. For $B_z < 0$ the FAC magnitude is smallest at noon and largest at dawn and dusk, with this trend reversed for $B_z > 0$, as expected from the representative patterns shown in Figure 1.

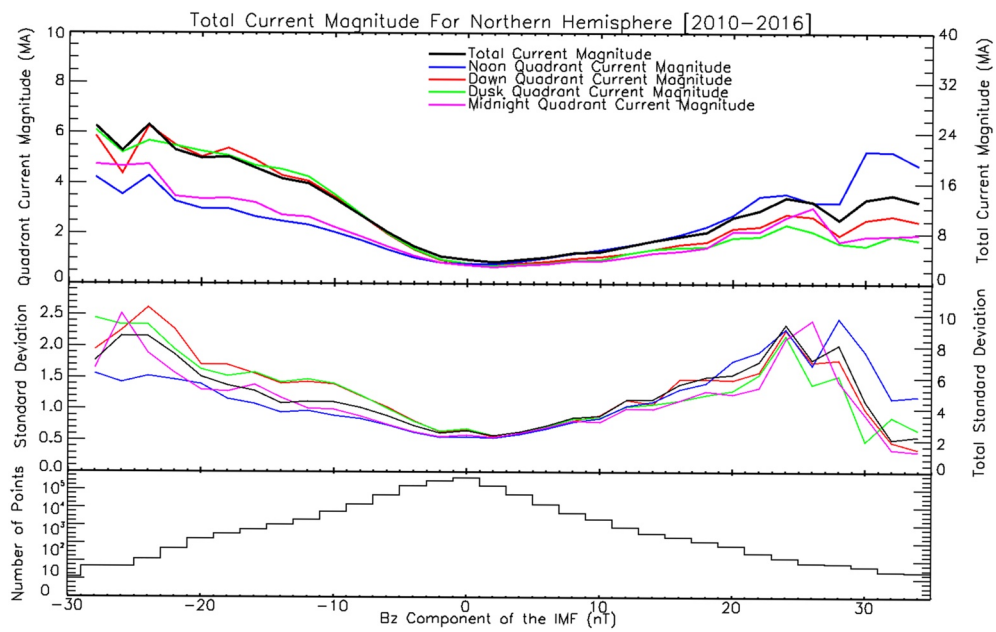

Figure 2. The top panel shows the total integrated current magnitudes (absolute magnitude of upwards and downwards flowing current summed), plotted against the corresponding value of interplanetary magnetic field B_z. The blue, pink, green and red shaded lines indicate the current magnitudes in the Noon, Midnight, Dusk and Dawn quadrants, respectively, with the left axis denoting scale. The black shaded line indicates the total current magnitude, with the right axis giving scale. The middle panel shows the standard deviations of each quadrant, with the same corresponding colors and format. The lower panel gives the number of data points for each bin.

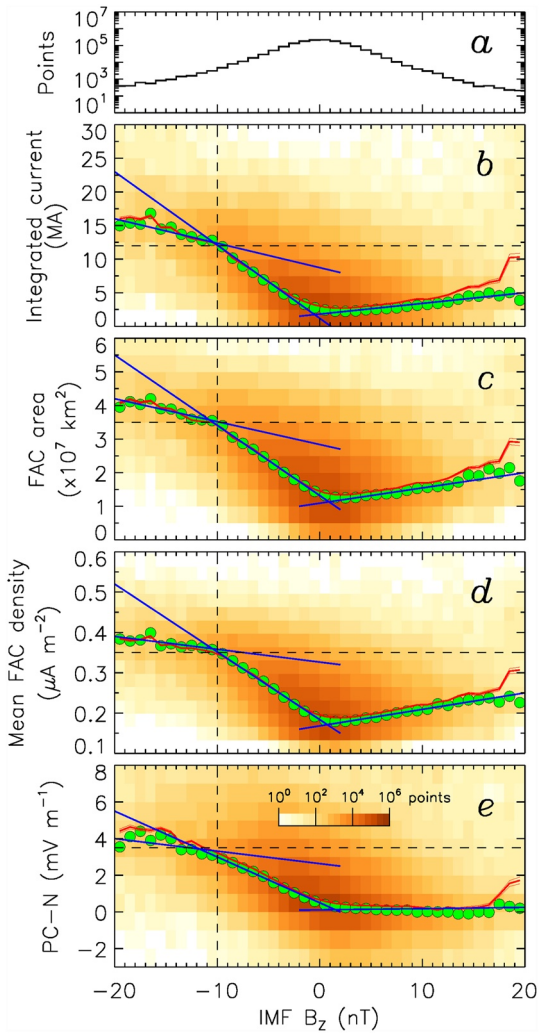

Figure 3. Field-aligned current (FAC) behavior as a function of the B_z component of the interplanetary magnetic field (IMF). Each panel shows 1 nT bins of B_z, with panel (a) indicating the number of data points present in each IMF B_z bin. Panels (b–e) show the total integrated current across the northern hemisphere of Earth, the area encompassed by these FACs, the mean FAC density (over the FAC area) and the PC-N index proxy of cross polar cap potential is given (respectively). In each panel, the sum of the magnitudes of upward and downward current is used to give the total integrated current, with the average then taken for each bin. The shaded orange- yellow coloring gives the distribution of data across the bins. The blue lines on panels (b–e) are superimposed to guide the eye to the linear behavior of the data, where applicable and the bold red lines give the mean. The thin red lines, above and below the mean line, give the standard deviation of each bin. The green markers denote the median of each bin.

In addition to this, the gradient is larger for $B_z < 0$, which again is to be expected. Despite the different rate of increase in the different quadrants, they all show the same quasi-linear trend, and so in the rest of the analysis we use the total FAC as the measure of current flow. During periods of northward IMF, the noon sector of each hemisphere was seen to provide the dominant contribution of current magnitude, as would be expected when considering the example shown in Figure 1 and the dynamics leading to high-latitude, dayside FACs during northward IMF. Consistency with Figure 1 is also demonstrated during periods of southward IMF. Here, the dawn and dusk quadrants were shown to provide the highest contribution to overall current magnitude for each hemisphere. It is worth noting that, in addition to B_z, all other upstream solar wind parameters considered in this study, followed the same behavior and evolution of that parameter between the quadrants. That is to say, the combined (total) all-quadrants FAC acts as a suitable proxy for all individual quadrant behaviors. For both northward and southward IMF, the increase in current magnitude with $|B_z|$ is roughly linear up to $|B_z| \pm 15$ nT. At higher values of B_z, the rate of increase does tend to decrease, but there is no abrupt plateau as seen in studies of CPCP saturation.

3.2. Solar Wind Parameters

The B_z component of the IMF is often considered the most important factor controlling the strength of the solar wind-magnetosphere interaction at Earth. In Figure 3 the behavior of the current magnitude is presented for instances of both northward (positive values) and southward (negative values) IMF polarity. The B_z range is limited to ±20 nT as beyond this there are too few observations, with less than 10 data points available during the years 2010–2016, to be statistically significant. The data are grouped into 1 nT bins and the total number of data points in each bin is indicated in panel a of Figure 3. The orange and yellow shading indicates the number of data points, with the scale given in panel e. Figure 3 also shows the variation of three FAC parameters with B_z: the total FAC integrated across the northern hemisphere, the area occupied by these FACs, the mean FAC density (integrated FAC divided by area), in panels b, c, and d, respectively. In each AMPERE map, we consider only grid cells with an absolute FAC density greater than 0.1 μA m^{-1}, which is at the noise floor of the AMPERE data set. We calculate the cross-sectional area occupied by those grid cells and the total absolute FAC (combining upward and downward FACs) and use this area to calculate the mean FAC density as the total integrated FAC divided by the area. This method was used as each the cells do not have a uniform contribution to the total average. The overall distribution of the data is shown by the shading, on a logarithmic scale. We also calculate the mean (thick red lines) and medians (green circles and diamonds for northward and southward IMF regimes, respectively) in each B_z bin. The thin red lines, above and below the mean line gives the standard deviation within each bin. In panel e we show the distribution of the PC-N index, which we use as a proxy for cross-polar cap potential (e.g., Milan et al., 2021). For positive B_z the total FAC, FAC area, and mean FAC density increase linearly with increasing B_z, but the variation is small. The PC-N variation shows no significant variation with positive B_z. A straight blue line is superimposed on the data to help guide the eye. The FAC quantities show a much stronger dependence on negative B_z, as is to be expected. The FAC area increases as the open flux in the polar cap increases, causing the auroral zone to expand to lower latitudes and to increase in latitudinal extent. The total FAC and mean FAC density also increase, as magnetospheric convection becomes more intense, resulting in stronger FACs that couple the magnetosphere and ionosphere. However, there are two distinct regimes in the behavior, with the increase being stronger for $B_z > -10$ nT and weaker for $B_z < -10$ nT.

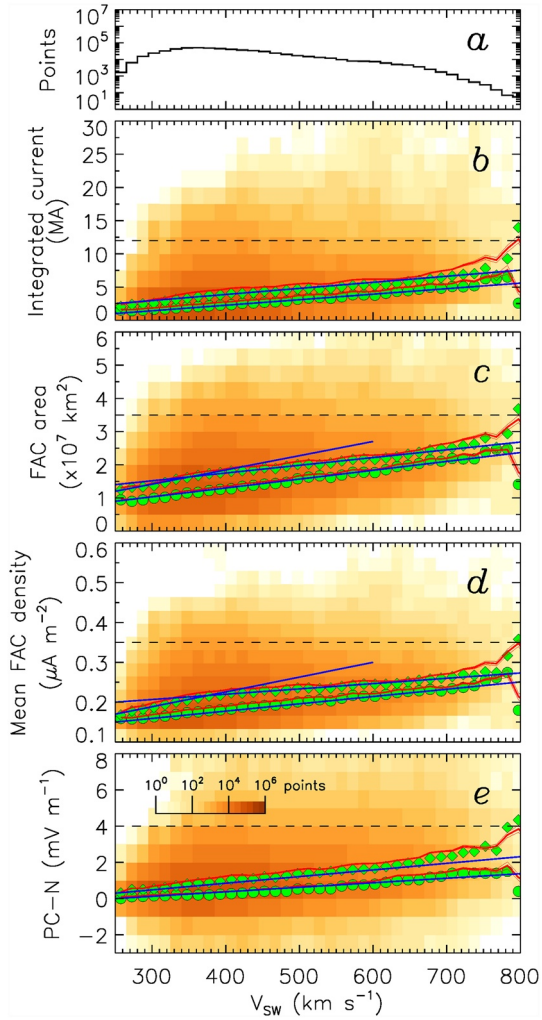

Figure 4. Field-aligned current variations with V_{sw} presented in a similar format to Figure 3. The data are subdivided into interplanetary magnetic field $B_z < 0$ (upper curve with green diamond markers) and $B_z > 0$ (lower curve with green circular markers) and separated into 15 km s^{-1} bins. The blue lines on the lower four panels are superimposed to guide the eye.

Two blue lines are superimposed to emphasize that the variation is approximately linear in the two regimes, with a distinct knee near $B_z = -10$ nT. PC-N also shows the same behavior, though the apparent dependence on IMF B_z above and below the knee is less pronounced. We note, returning to Figure 2, that the knee in the variation of FAC magnitude with negative B_z is apparent in all the individual quadrants as well as the total.

Figure 4, in the same format as Figure 3, shows the evolution of the same three FAC parameters with increasing solar wind speed. The upper and lower lines show the variation for southward and northward IMF data, indicated by the green diamond and circle markers, respectively.

The shading indicates the overall distribution of the data, but the mean and medians have been subdivided into IMF $B_z < 0$ (upper curves with diamond shaped markers) and $B_z > 0$ (lower curves with circular shaped markers). The dependence of the FAC parameters on V_{sw} are modest; note that the vertical scales are the same in Figures 3–7, indicating the V_{sw} does not order the data particularly well. There is some indication of a knee in the $B_z < 0$ curves of FAC area and density near V_{sw} of 400 km/s, but this is not particularly pronounced. The trend becomes less clear above 700 km/s due to a paucity of data points.

Figure 5 shows the results ordered by N_{sw} for $B_z < 0$ (upper, diamond shaped markers) and $B_z > 0$ (lower, circular shaped markers). As with V_{sw}, the variation of the FAC quantities with N_{sw} is modest and largely linear. The PC-N index has a low dependence with N_{sw}, however a modest, positive linear relationship is discernible.

Figure 6 presents the variations with E_{sw}. The trends are similar to Figure 3. For $E_{sw} < 0$ ($B_z > 0$), total FAC, FAC area, and FAC density all rise slowly and linearly as the magnitude of E_{sw} increases. For $E_{sw} > 0$, the rise is steeper as the magnitude of E_{sw} increases, but with a distinct knee near $E_{sw} = 4$ mV/m, with a slower climb beyond that. Figure 7 presents the relationship of FACs and PC-N to the coupling parameter shown in Equation 1, in a similar format to previous figures. Figure 7 combines both $B_z > 0$ and $B_z < 0$ values, though $B_z > 0$ will generally give low values of Φ_D and $B_z > 0$ will give higher values due to the dependence on the IMF clock angle (i.e., the $\sin^{\frac{9}{2}}\frac{1}{2}\theta$ term in Equation 1). As in previous figures, a clear knee is seen in all parameters near 80–100 kV.

The solar wind dynamic pressure (P_{sw}) is given in Figure 8. The increase in P_{sw} shows a knee feature, which has been highlighted on the negative B_z trace (denoted by the diamond markers). It is worth noting here that the linear lines, drawing the eye to the two different regimes of increases is only plotted on the upper curve (southward, diamond marker indicated, IMF), for clarity. The ratio between the two regimes and the linear lines themselves were very similar for both northward and southward IMF.

In many of the presented cases, for IMF $B_z < 0$ there is a distinct knee in the rate of increase in the FAC parameters with increasing solar wind driving. We now compare the rate of increase below the knee (rapid) with the rate above the knee (slow) by taking the ratio of the gradients of the blue lines fitted above and below the knee. The larger this number, the more distinct is the change in dependencies of FAC parameters on upstream driving conditions. The results are presented in Table 1.

Across Φ_D, B_z, and E_{sw}, the FAC area saw a linearity change ratio of approximately 3. The total integrated current ratio is given to be around 2 for both Φ_D and E_{sw}, however for B_z and P_{sw} the ratio reached 3.0 and 5.8, respectively. This difference in behavior of B_z and P_{sw} is also seen in the current density, where the ratios are all generally higher across all parameters, with P_{sw} and B_z still exceeding the values of the other two parameters. The current

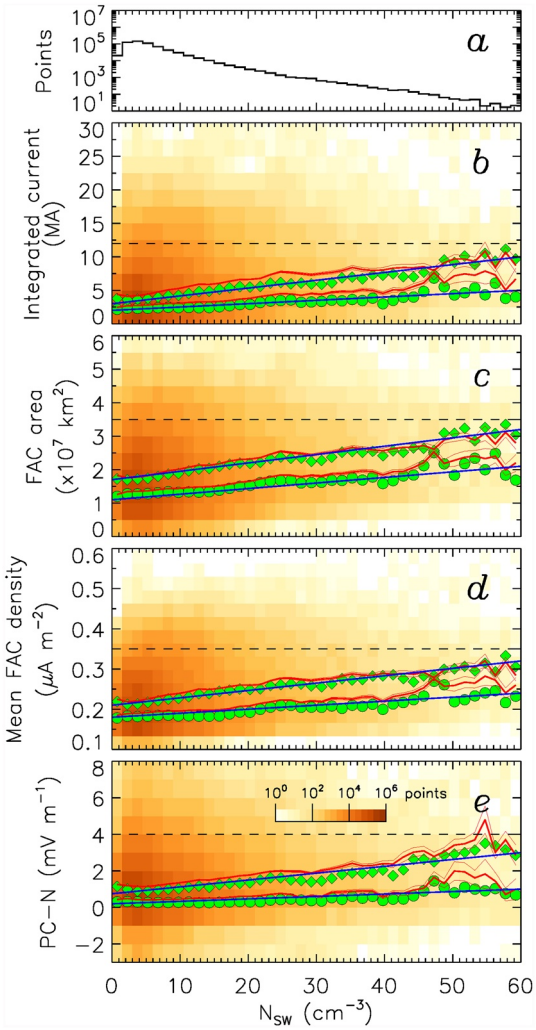

Figure 5. Field-aligned current variations with N_{sw} presented in a similar format to Figure 3. The data are subdivided into interplanetary magnetic field $B_z < 0$ (upper curve with diamond markers) and $B_z > 0$ (lower curve with circular markers). Current magnitude behavior is separated into 1.5 cm^{-3} bins with standard deviation values given in the thin red lines above and below the average bin value (thick red line). The blue lines on the lower four panels are superimposed to guide the eye.

area shows the most variability between the three parameters with just 2.8 for E_{sw} and 7.6 for P_{sw}. While P_{sw} and B_z both show a higher change between the pre and post knee regimes, P_{sw} certainly gives the most variation. This is particularly interesting as the constituent parameters of P_{sw} (N_{sw} and V_{sw}) both show no knee feature.

4. Discussion

Within this study, we have investigated how integrated FAC magnitude, area and mean density vary with a variety of solar wind parameters including solar wind speed, density, electric field, B_z component of the IMF and a proxy for solar wind driving (Milan et al. (2012) coupling parameter). During the initial stages of the investigation, the FACs were analyzed in 4 separate MLT quadrants in order to identify any unique behavior of specific current systems, indicated by evolution of current within the specific MLT region. After reviewing each upstream solar wind parameter considered it was found that the resulting current magnitudes in each quadrant, while each having different magnitude contributions to the total, (as would be expected), showed no significant or unique behaviors in any individual MLT quadrant. This uniformity in current evolution allowed the total integrated current across each hemisphere to be used for the analysis. These total current results show that, as the solar wind driving increases and becomes more intense, both the area and the mean density of the FACs increase, aligning with the conclusions of previous studies and widely accepted theory (Clausen et al., 2012; Coxon et al., 2014a; Iijima & Potemra, 1978). The increase in area arises as the FACs move to lower latitudes and have a greater latitudinal width. The increase in FAC density can be attributed to increased coupling at the nose of the magnetosphere increasing open flux and more activity occurring within the magnetotail, resulting in increased particle precipitation and faster ionospheric convection overcoming frictional drag with the atmosphere. This result falls into good agreement with accepted theory, first outlined in the work of Clausen et al. (2012) and Clausen et al. (2013a, 2013b) and also by Coxon et al. (2014a, 2014b). While we have employed the Milan et al. (2012) coupling parameter, other coupling parameters have been presented in previous studies, such as the ϵ parameter given in work by Perrault and Akasofu (1978), in addition to the Newell et al. (2007) "almost universal" coupling parameter. Future work may could perform similar analyses using these, and other, coupling parameters in order to gain a greater understanding of how the trends vary when incorporating different proxies for solar wind driving, in different configurations in terms of solar wind parameters. In this way, we could expand Borovsky (2021), who looked into the varying components of CPCP saturation.

The solar wind parameters and PC-N have a linear relationship with solar wind speed, V_{sw}. This may suggest that the magnetic field, especially the B_z component is more important in the control of this driving of the FACs. In addition, during periods of northwards IMF (when $B_z > 0$), the FACs increase linearly for stronger B_z and also E_{sw} however this increase is also low. The area of the FACs remains generally quite low, as they are largely confined to the noon sector (as outlined by Figure 1), where lobe reconnection drives reverse convection (Iijima & Shibaji, 1987; Iijima et al., 1984; Imber et al., 2006; Weimer, 2001; Zanetti et al., 1984). The increase in E_{sw} is also seen to be stronger than that of B_z, indicating that the combination of B_z and V_{sw} has greater significance in the driving of lobe reconnection. In addition, it is interesting to note that, while the knee feature is not seen in N_{sw} or V_{sw}, it is evident in the P_{sw} evolution. For all values of $B_z > 0$ (and $E_{sw} < 0$), PC-N remains close to zero. This suggests that PC-N is a poor measure of reverse lobe convection in the noon sector, perhaps due to it being mainly measured within the central polar cap. For $B_z < 0$, the FACs and PC-N increase more strongly, however there is a distinct knee in the variation with B_z, E_{sw} and Φ_D, near −10 nT, 4 mV/m and 90 kV, respectively in

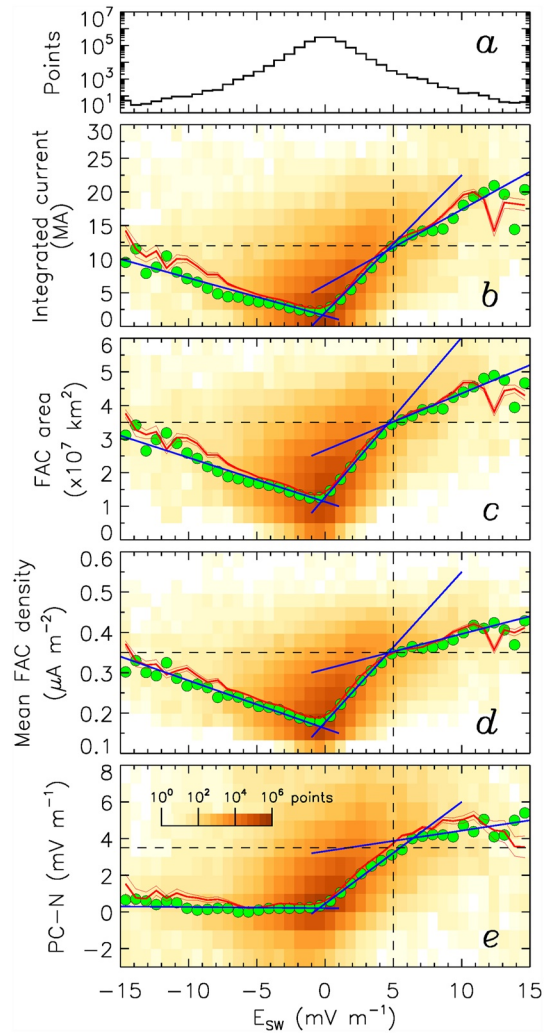

Figure 6. Field-aligned current variations with E_{sw} presented in a similar format to Figure 3. The data are subdivided into interplanetary magnetic field $B_z < 0$ (positive E_{sw}) and $B_z > 0$ (negative E_{sw}). Current magnitude behavior for northwards is separated into 0.75 mV m^{-1} bins with standard deviation values given in the thin red lines above and below the average bin value (thick red line). The blue lines on the lower four panels are superimposed to guide the eye.

each case. These are approximately consistent as combined values of solar wind speed and IMF B_z of 400 km s^{-1} and −10 nT correspond to an E_{sw} of 4 mV/m. The shape of the curves is also approximately consistent with the Hill-Siscoe model presented in Hairston et al. (2005). For the B_z, E_{sw}, and Φ_D parameters, the ratio of the gradients of the blue lines tends to be greatest for FAC density, that is to say that the "saturation" for this parameter is sharpest, rather than the area or total magnitudes. This could be suggestive that the magnetosphere-ionosphere coupling is limited by the capacity of the magnetosphere to carry current in a given area.

In Figures 6 and 7, the FACs do not appear to saturate for $B_z > 0$, as they do for $B_z < 0$. In one regard, $B_z < 0$ does not see the integrated FAC magnitudes and densities reaching as high as the knee feature seen for $B_z < 0$, which may mean they do not reach their limiting value. This is supported by the work of Wilder et al. (2008), which verified a CPCP saturation during $B_z > 0$ conditions. On the other hand, the Hill-Siscoe model suggests that saturation is caused by a deformation of magnetic structure, and hence reconnection rates, by intense R1 currents, and these are only present for $B_z < 0$. Future work could look at this in more detail by investigating the R1 FACs in isolation and their relationship to other FACs, perhaps using the principal component analysis technique of Milan et al. (2015). Turning our attention now to the PC-N index, this does not increase with N_{sw}, as predicted by Milan et al. (2012). However, FAC parameters do increase marginally, suggesting that the compression of the magnetosphere somewhat enhances the FACs. Work undertaken by Wang et al. (2006) and Nakano et al. (2009)

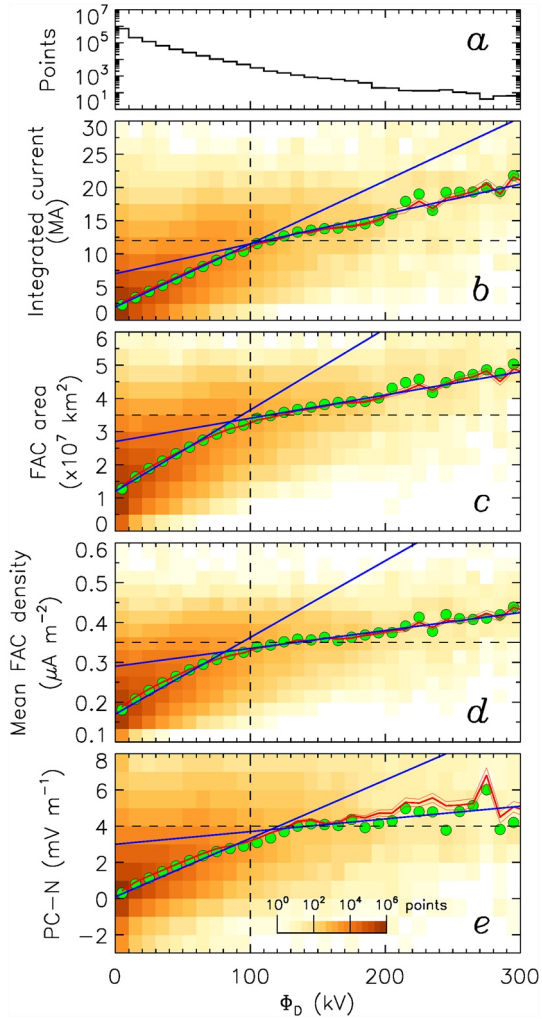

Figure 7. Field-aligned current variations with Φ_D, given by the Milan et al. (2012) coupling parameter, presented in a similar format to Figure 3. The Φ_D data are separated into 10 kV bins and the blue lines on the lower four panels are superimposed to guide the eye.

also found a link between solar wind pressure and FAC density, supporting this finding. In addition, this may explain why some coupling parameters find a link between geomagnetic activity and N_{sw} which is not an effect of increased reconnection.

It is important to consider the dynamics of how the FACs are driven when looking at the values within Table 1. Table 1 gives insight into the knee feature seen in the four parameters listed, across all the current values. In particular, the current density shows a consistently high knee feature for all parameters within the table. This would infer that in general, the current density often shows a significant difference in magnitude between the two regimes (before and after the knee feature) for these solar wind parameters (B_z, E_{sw}, P_{sw}, and Φ_D). P_{sw} has a high ratio for all parameters, except for a moderate value for PC-N. The solar wind pressure, particularly in the form of pressure pulses, can drive FAC magnitudes and, as such, these high ratios would suggest that this driving can offer a modest contribution, however is limited and will cease to provide additional contributions after the magnitude at which the knee feature occurs. P_{sw} shows the most consistently high change due to the knee feature seen, except for PC-N, indicative of a low dependency of PC-N on *Psw*. In contrast, the lower ratio values for B_z, such as that for PC-N, are representative of a consistently high dependency on B_z, that continues throughout the knee feature.

5. Conclusion

In this paper we have presented our investigations into saturation across the large-scale FACs of Earth. By using AMPERE data to calculate the total integrated current in each hemisphere, we have analyzed the extent of FAC saturation in relation to the upstream solar wind conditions, including parameters such as solar wind speed, density, pressure, B_z component of the IMF, E_{sw} and the Milan et al. (2012) coupling parameter. The currents themselves were also further analyzed in terms of total current, mean current density, area over which they cover and also the PC-N index (a proxy for cross-polar cap potential, itself a proxy for the dayside reconnection rate). Consideration was taken to resolve any unique features that may appear in the evolution of the current systems. This was achieved by considering each current system for both northward and southward IMF conditions and based on MLT location. It was concluded, after investigating each parameter, that despite expected differences in overall magnitude, no individual current systems showed any evolution behavior that would be lost by using the total integrated current. In some cases, a distinct knee is seen in the variations, above which the rate of increase with solar wind driver decreases, which we refer to as "saturation," though the observations do not. That is to say that, despite the knee feature present in some cases, the parameters do not exhibit the same complete saturation expected from previous studies (Hairston et al., 2005; Russell et al., 2001; Shepherd, 2007) This knee is seen for Φ_D, $B_z < 0$, E_{SW} (for $B_z < 0$), and to a lesser degree P_{sw}. These knees occur at $\Phi_D = 100$ kV, $B_z = -10$ nT, $E_{sw} = 4$ mV/m, and $P_{sw} = 5$ nPa. In all cases, the knees correspond to $I = 12$ MA, $A = 3 \times 10^7$ km^2, $j = 0.35$ μA m^{-2}, and PC-$N = 3$ mV m^{-1}. Those solar wind parameters for which saturation is not seen ($B_z > 0$, E_{SW} for $B_z > 0$, N_{sw}, and V_{sw}) do not produce I, A, j, or PC-N which exceed the threshold for saturation. It is interesting to consider if saturation would be seen for, say, $E_{SW} < 0$ (i.e., $B_z > 0$) if there was sufficient data to extend the range of Figure 6, beyond $E_{SW} < -15$ mV m^{-1}, where an extrapolation of the trends suggests the thresholds of I, A, and j would be exceeded. With the results gathered within this study, the question of what causes the saturation effect can be considered. Activity within the magnetosphere, including magnetospheric/ionospheric convection, is primarily driven by reconnection occurring at the magnetopause. Past studies have shown that the cross-polar cap potential tends to saturate for large values of E_{sw}, as we confirm in this study. This

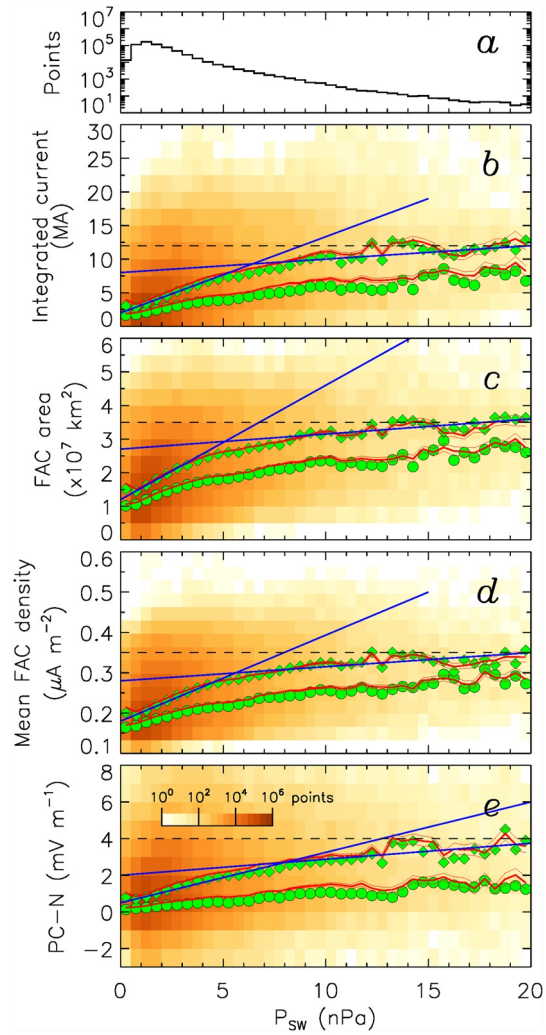

Figure 8. Field-aligned current variations with P_{sw}, presented in a similar format to Figure 3. The *Psw* data are separated into 0.5 nPa bins and the blue lines on panels (b–e) are superimposed to guide the eye.

suggests that on average the reconnection process is limited when solar wind conditions become extreme, for example, $B_z < -10$ nT. Siscoe et al. (2002) argued that when the R1 FAC system grows too large it weakens the magnetic field at the magnetopause, limiting the reconnection rate. This would only be expected to occur for $B_z < 0$ as the reconnection geometry is significantly different for $B_z > 0$ (reconnection occurring near the cusps rather than at low latitudes) and the R1 FAC system is not significantly driven for $B_z > 0$. This tallies with our observations, in which the FAC magnitude is weak and saturation is not observed for$B_z > 0$. The magnitude of the FACs is controlled by two factors: the rate of magnetospheric convection and the ionospheric conductance. The latter is seasonally dependent due to changing levels of insolation of the polar regions (e.g., Milan et al., 2017). Also, for poorly understood reasons, FACs tend to be stronger in the northern hemisphere than the southern hemisphere (Coxon et al., 2016). An avenue for further research is to search for a seasonal dependence in saturation, due to the changing strengths in the R1 FAC system, which are themselves different in the two hemispheres. Indeed, rather than quantifying the total integrated FAC, it would be interesting to isolate the R1 FACs within the AMPERE observations (for instance, using techniques similar to those of Milan et al. (2015)) to study the dependence of saturation on just that current system.

Table 1
Ratio of Linear Line Fits for Each Parameter Regime

	Φ_D	B_z	E_{sw}	P_{sw}
Area	3.6	3.1	2.8	7.6
Total	2.1	3.0	1.8	5.8
Density	4.3	5.3	4.3	6.0
PC-N	4.6	3.7	4.9	3.1

Data Availability Statement

The data used withing this study can be found in two separate databases. First, the 1-min resolution solar wind data used can be accessed from OMNIWeb via the link https://omniweb.gsfc.nasa.gov/form/omni_min.html (OMNIWeb data explorer, 2023). The 2-min resolution current map data (AMPERE data) can be retrieved from https://ampere.jhuapl.edu/download/ (Custom fitted data, 2023) with additional tools to help utilize the data available under the "data tools" tab. In addition, we would like to acknowledge that this research used the SPECTRE High Performance Computing Facility at the University of Leicester. Finally, the authors would like to thank all the teams involved in providing and managing the data and computing services used within this study.

Acknowledgments
A. Fleetham was able to undertake this study, with the support of the co-authors listed, under the financial support of a studentship provided by the Science and Technology facilities council (STFC) as part of UK Research and Innovation (UKRI), ST/T506242/1. Further financial support is provided by STFC as part of the consolidated Grant ST/W00089X/1.

References

Anderson, B. J., Angappan, R., Barik, A., Vines, S. K., Stanley, S., Bernasconi, P. N., et al. (2021). Iridium communications satellite constellation data for study of earth's magnetic field. *Geochemistry, Geophysics, Geosystems*, *22*(8), e2020GC009515. https://doi.org/10.1029/2020GC009515

Anderson, B. J., & Korth, H. (2007). Saturation of global field aligned currents observed during storms by the iridium satellite constellation. *Journal of Atmospheric and Solar-Terrestrial Physics*, *69*(1), 166–169. https://doi.org/10.1016/j.jastp.2006.06.013

Anderson, B. J., Korth, H., Waters, C. L., Green, D. L., Merkin, V. G., Barnes, R. J., & Dyrud, L. P. (2014). Development of large-scale Birkeland currents determined from the active magnetosphere and planetary electrodynamics response experiment. *Geophysical Research Letters*, *41*(9), 3017–3025. https://doi.org/10.1002/2014GL059941

Anderson, B. J., Korth, H., Waters, C. L., Green, D. L., & Stauning, P. (2008). Statistical Birkeland current distributions from magnetic field observations by the iridium constellation. *Annales Geophysicae*, *26*(3), 671–687. https://doi.org/10.5194/angeo-26-671-2008

Anderson, B. J., Takahashi, K., Kamei, T., Waters, C. L., & Toth, B. A. (2002). Birkeland current system key parameters derived from iridium observations: Method and initial validation results. *Journal of Geophysical Research*, *107*(A6), SMP11-1–SMP11-13. https://doi.org/10.1029/2001JA000080

Birkeland, K. (1908). *The Norwegian aurora polaris expedition 1902-1903* (Vol. 1). H. Aschelhoug and Company.

Birkeland, K. (1913). *The Norwegian aurora polaris expedition 1902-1903* (Vol. 3). H. Aschelhoug and Company.

Borovsky, J. E. (2021). On the saturation (or not) of geomagnetic indices. *Frontiers in Astronomy and Space Sciences*, *8*, 740811. https://doi.org/10.3389/fspas.2021.740811

Carter, J. A., Milan, S. E., Coxon, J. C., Walach, M.-T., & Anderson, B. J. (2016). Average field-aligned current configuration parameterized by solar wind conditions. *Journal of Geophysical Research: Space Physics*, *121*(2), 1294–1307. https://doi.org/10.1002/2015JA021567

Clausen, L. B. N., Baker, J. B. H., Ruohoniemi, J. M., Milan, S. E., & Anderson, B. J. (2012). Dynamics of the region 1 Birkeland current oval derived from the active magnetosphere and planetary electrodynamics response experiment (ampere). *Journal of Geophysical Research*, *117*(A6), A06233. https://doi.org/10.1029/2012JA017666

Clausen, L. B. N., Baker, J. B. H., Ruohoniemi, J. M., Milan, S. E., Coxon, J. C., Wing, S., et al. (2013a). Temporal and spatial dynamics of the regions 1 and 2 Birkeland currents during substorms. *Journal of Geophysical Research: Space Physics*, *118*(6), 3007–3016. https://doi.org/10.1002/jgra.50288

Clausen, L. B. N., Milan, S. E., Baker, J. B. H., Ruohoniemi, J. M., Glassmeier, K.-H., Coxon, J. C., & Anderson, B. J. (2013b). On the influence of open magnetic flux on substorm intensity: Ground- and space-based observations. *Journal of Geophysical Research: Space Physics*, *118*(6), 2958–2969. https://doi.org/10.1002/jgra.50308

Cowley, S. W. H., & Lockwood, M. (1992). Excitation and decay of solar wind-driven flows in the magnetosphere-ionosphere system. *Annales Geophysicae*, *10*, 103–115. Retrieved from https://ui.adsabs.harvard.edu/abs/1992AnGeo..10..103C

Coxon, J. C., Milan, S. E., carter, J. A., Clausen, L. B. N., Anderson, B. J., & Korth, H. (2016). Seasonal and diurnal variations in ampere observations of the Birkeland currents compared to modeled results. *Journal of Geophysical Research: Space Physics*, *121*(5), 4027–4040. https://doi.org/10.1002/2015JA0220502169-9402

Coxon, J. C., Milan, S. E., Clausen, L. B. N., Anderson, B. J., & Korth, H. (2014a). The magnitudes of the regions 1 and 2 Birkeland currents observed by ampere and their role in solar wind-magnetosphere-ionosphere coupling. *Journal of Geophysical Research: Space Physics*, *119*(12), 9804–9815. https://doi.org/10.1002/2014JA020138

Coxon, J. C., Milan, S. E., Clausen, L. B. N., Anderson, B. J., & Korth, H. (2014b). A superposed epoch analysis of the regions 1 and 2 Birkeland currents observed by ampere during substorms. *Journal of Geophysical Research: Space Physics*, *119*(12), 9834–9846. https://doi.org/10.1002/2014JA020500

Cummings, W. D., & Dessler, A. J. (1967). Field-aligned currents in the magnetosphere. *Journal of Geophysical Research*, *72*(3), 1007–1013. https://doi.org/10.1029/JZ072i003p01007

Custom Fitted Data. (2023). AMPERE. Retrieved from https://ampere.jhuapl.edu/download/

Dungey, J. W. (1961). Interplanetary magnetic field and the auroral zones. *Physical Review Letters*, *6*(2), 47–48. https://doi.org/10.1103/PhysRevLett.6.47

Erickson, G. M., Spiro, R. W., & Wolf, R. A. (1991). The physics of the Harang discontinuity. *Journal of Geophysical Research*, *96*(A2), 1633–1645. https://doi.org/10.1029/90JA02344

Fear, R. C. (2021). The northward IMF magnetosphere. In *Magnetospheres in the solar system* (pp. 293–309). https://doi.org/10.1002/9781119815624.ch19

Fuselier, S. A. (2021). Dayside magnetopause processes. In *Magnetospheres in the solar system* (pp. 153–161). https://doi.org/10.1002/9781119815624.ch10

Ganushkina, N. Y., Liemohn, M. W., & Dubyagin, S. (2018). Current systems in the earth's magnetosphere. *Reviews of Geophysics*, *56*(2), 309–332. https://doi.org/10.1002/2017RG000590

Gao, Y., Kivelson, M. G., & Walker, R. J. (2013). Two models of cross polar cap potential saturation compared: Siscoe-Hill model versus Kivelson-Ridley model. *Journal of Geophysical Research: Space Physics*, *118*(2), 794–803. https://doi.org/10.1002/jgra.50124

Hairston, M. R., Drake, K. A., & Skoug, R. (2005). Saturation of the ionospheric polar cap potential during the October–November 2003 superstorms. *Journal of Geophysical Research*, *110*(A9), A09S26. https://doi.org/10.1029/2004JA010864

Iijima, T., & Potemra, T. A. (1976). The amplitude distribution of field-aligned currents at northern high latitudes observed by triad (Report).

Iijima, T., & Potemra, T. A. (1978). Large-scale characteristics of field-aligned currents associated with substorms. *Journal of Geophysical Research*, *83*(A2), 599–615. https://doi.org/10.1029/JA083iA02p00599

Iijima, T., Potemra, T. A., Zanetti, L. J., & Bythrow, P. F. (1984). Large-scale Birkeland currents in the dayside polar region during strongly northward IMF: A new Birkeland current system. *Journal of Geophysical Research*, *89*(A9), 7441–7452. https://doi.org/10.1029/JA089iA09p07441

Iijima, T., & Shibaji, T. (1987). Global characteristics of northward IMF-associated (NBZ) field-aligned currents. *Journal of Geophysical Research*, *92*(A3), 2408–2424. https://doi.org/10.1029/JA092iA03p02408

Imber, S. M., Milan, S. E., & Hubert, B. (2006). The auroral and ionospheric flow signatures of dual lobe reconnection. *Annales Geophysicae*, *24*(11), 3115–3129. https://doi.org/10.5194/angeo-24-3115-2006

Khachikjan, G. Y., Koustov, A. V., & Sofko, G. J. (2008). Dependence of SuperDARN cross polar cap potential upon the solar wind electric field and magnetopause subsolar distance: Cross-polar cap potential saturation. *Journal of Geophysical Research*, *113*(A9), A09214. https://doi.org/10.1029/2008JA013107

King, J. H., & Papitashvili, N. E. (2005). Solar wind spatial scales in and comparisons of hourly wind and ace plasma and magnetic field data. *Journal of Geophysical Research*, *110*(A2), A02104. https://doi.org/10.1029/2004JA010649

Kivelson, M. G., & Ridley, A. J. (2008). Saturation of the polar cap potential: Inference from Alfvén wing arguments. *Journal of Geophysical Research*, *113*(A5), A05214. https://doi.org/10.1029/2007JA012302

Milan, S. E., Carter, J. A., Sangha, H., Bower, G. E., & Anderson, B. J. (2021). Magnetospheric flux throughput in the Dungey cycle: Identification of convection state during 2010. *Journal of Geophysical Research: Space Physics*, *126*(2), e2020JA028437. https://doi.org/10.1029/2020JA028437

Milan, S. E., Carter, J. A., Bower, G. E., Imber, S. M., Paxton, L. J., Anderson, B. J., et al. (2020). Dual-lobe reconnection and horse-collar auroras. *Journal of Geophysical Research: Space Physics*, *125*(10), e2020JA028567. https://doi.org/10.1029/2020JA028567

Milan, S. E., Carter, J. A., Korth, H., & Anderson, B. J. (2015). Principal component analysis of Birkeland currents determined by the active magnetosphere and planetary electrodynamics response experiment: Principal component analysis of facts. *Journal of Geophysical Research: Space Physics*, *120*(12), 10–10424. https://doi.org/10.1002/2015JA021680

Milan, S. E., Clausen, L. B. N., Coxon, J. C., Carter, J. A., Walach, M. T., Laundal, K., et al. (2017). Overview of solar wind–magnetosphere–ionosphere–atmosphere coupling and the generation of magnetospheric currents. *Space Science Reviews*, *206*(1–4), 547–573. https://doi.org/10.1007/s11214-017-0333-0

Milan, S. E., Gosling, J. S., & Hubert, B. (2012). Relationship between interplanetary parameters and the magnetopause reconnection rate quantified from observations of the expanding polar cap. *Journal of Geophysical Research*, *117*(A3), A03226. https://doi.org/10.1029/2011JA017082

Nakano, S., Ueno, G., Ohtani, S., & Higuchi, T. (2009). Impact of the solar wind dynamic pressure on the region 2 field-aligned currents. *Journal of Geophysical Research*, *114*(A2), A02221. https://doi.org/10.1029/2008JA013674

Newell, P. T., Sotirelis, T., Liou, K., Meng, C. I., & Rich, F. J. (2007). A nearly universal solar wind-magnetosphere coupling function inferred from 10 magnetospheric state variables. *Journal of Geophysical Research*, *112*(A1), A01206. https://doi.org/10.1029/2006JA012015

Ohtani, S., Potemra, T. A., Newell, P. T., Zanetti, L. J., Iijima, T., Watanabe, M., et al. (1995). Four large-scale field-aligned current systems in the dayside high-latitude region. *Journal of Geophysical Research*, *100*(A1), 137–153. https://doi.org/10.1029/94JA01744

OMNIWeb Data Explorer. (2023). NASA. Retrieved from https://omniweb.gsfc.nasa.gov/form/omni_min.html

Perrault, P., & Akasofu, S.-I. (1978). A study of geomagnetic storms. *Geophysics Journal of the Royal Astronomical Society Special Publications*, *54*(3), 547–573. https://doi.org/10.1111/j.1365-246x.1978.tb05494.x

Russell, C. T., Luhmann, J. G., & Lu, G. (2001). Nonlinear response of the polar ionosphere to large values of the interplanetary electric field. *Journal of Geophysical Research*, *106*(A9), 18495–18504. https://doi.org/10.1029/2001JA900053

Saunders, M. A. (1989). Origin of the cusp Birkeland currents. *Geophysical Research Letters*, *16*(2), 151–154. https://doi.org/10.1029/GL016i002p00151

Shepherd, S. G. (2007). Polar cap potential saturation: Observations, theory, and modeling. *Journal of Atmospheric and Solar-Terrestrial Physics*, *69*(3), 234–248. https://doi.org/10.1016/j.jastp.2006.07.022

Siscoe, G. L., Erickson, G. M., Sonnerup, B. U., Maynard, N. C., Schoendorf, J. A., Siebert, K. D., et al. (2002). Hill model of transpolar potential saturation: Comparisons with MHD simulations. *Journal of Geophysical Research*, *107*(A6), SMP8-1–SMP8-8. https://doi.org/10.1029/2001JA000109

Siscoe, G. L., & Huang, T. S. (1985). Polar cap inflation and deflation. *Journal of Geophysical Research*, *90*(A1), 543–547. https://doi.org/10.1029/JA090iA01p00543

Wang, H., Lühr, H., Ma, S. Y., Weygand, J., Skoug, R. M., & Yin, F. (2006). Field-aligned currents observed by champ during the intense 2003 geomagnetic storm events. *Annales Geophysicae*, *24*(1), 311–324. https://doi.org/10.5194/angeo-24-311-2006

Waters, C. L., Anderson, B. J., Green, D. L., Korth, H., Barnes, R. J., & Vanhamäki, H. (2020). Science data products for ampere. In M. W. Dunlop, & H. Lühr (Eds.), *Ionospheric multi-spacecraft analysis tools: Approaches for deriving ionospheric parameters* (pp. 141–165). Springer International Publishing. https://doi.org/10.1007/978-3-030-26732-2_7

Waters, C. L., Anderson, B. J., Greenwald, R. A., Barnes, R. J., & Ruohoniemi, J. M. (2004). High-latitude poynting flux from combined iridium and SuperDARN data. *Annales Geophysicae*, *22*(8), 2861–2875. https://doi.org/10.5194/angeo-22-2861-2004

Waters, C. L., Anderson, B. J., & Liou, K. (2001). Estimation of global field aligned currents using the iridium® system magnetometer data. *Geophysical Research Letters*, *28*(11), 2165–2168. https://doi.org/10.1029/2000GL012725

Weimer, D. R. (2001). Maps of ionospheric field-aligned currents as a function of the interplanetary magnetic field derived from dynamics explorer 2 data. *Journal of Geophysical Research*, *106*(A7), 12889–12902. https://doi.org/10.1029/2000JA000295

Wilder, F. D., Clauer, C. R., & Baker, J. B. H. (2008). Reverse convection potential saturation during northward IMF: Reverse convection saturation. *Geophysical Research Letters*, *35*(12), L12103. https://doi.org/10.1029/2008GL034040

Zanetti, L. J., Potemra, T. A., Iijima, T., Baumjohann, W., & Bythrow, P. F. (1984). Ionospheric and Birkeland current distributions for northward interplanetary magnetic field: Inferred polar convection. *Journal of Geophysical Research*, *89*(A9), 7453–7458. https://doi.org/10.1029/JA089iA09p07453